9-12 AUGUST 2015
inter.noise 2015
SAN FRANCISCO, CALIFORNIA USA

A method for simulation of rotorcraft fly-in noise for human response studies

Stephen A. Rizzi[a]
Aeroacoustics Branch, NASA Langley Research Center
Hampton, Virginia, 23681, USA

Andrew Christian[b]
Structural Acoustics Branch, NASA Langley Research Center
Hampton, Virginia, 23681, USA

The low frequency content of rotorcraft noise allows it to be heard over great distances. This factor contributes to the disruption of natural quiet in national parks and wilderness areas, and can lead to annoyance in populated areas. Further, it can result in detection at greater distances compared to higher altitude fixed wing aircraft operations. Human response studies conducted in the field are made difficult since test conditions are difficult to control. Specifically, compared to fixed wing aircraft, the source noise itself may significantly vary over time even for nominally steady flight conditions, and the propagation of that noise is more variable due to low altitude meteorological conditions. However, it is possible to create the salient features of rotorcraft fly-in noise in a more controlled laboratory setting through recent advancements made in source noise synthesis, propagation modeling and reproduction. This paper concentrates on the first two of these. In particular, the rotorcraft source noise pressure time history is generated using single blade passage signatures from the main and tail rotors. These may be obtained from either acoustic source noise predictions or back-propagation of ground-based measurements. Propagation effects include atmospheric absorption, spreading loss, Doppler shift, and ground plane reflections.

1 INTRODUCTION

Noise from low flying rotorcraft is a source of annoyance in both natural and populated areas and is the impetus for recent rules affecting their operations.[1-3] For rotorcraft noise to be judged as annoying, it must first be audible. Validation of human aural detection models,[4-6] whether they be based on field observations[7, 8] or more fundamental work,[9] is difficult to accomplish using sound jury data acquired in field tests. This is because unsteadiness associated with both the source and

[a] email: stephen.a.rizzi@nasa.gov
[b] email: andrew.christian@nasa.gov

long propagation path negatively affect repeatability and controllability, and introduce uncertainty. In addition, such testing can only be conducted on an already developed vehicle, limiting the ability to assess the effect of design or operational changes on the audibility.

This paper describes a method for simulation of rotorcraft fly-in noise for use in audibility studies. The approach taken synthesizes the source noise pressure time history using available source noise data, and uses physical models to propagate the sound to a distant observer. In doing so, it purposefully eliminates the source and path unsteadiness, resulting in a monotonically increasing level on approach, and making future validation of detection models via laboratory sound jury testing more tractable.

2 SOURCE NOISE SYNTHESIS

The source noise synthesis is comprised of two parts. The first part entails the source noise description and the second part entails generation of the source noise pressure time history based on that description. Only the main and tail rotor sources are considered herein as these dominate the audibility of an approaching rotorcraft. Other sources such as turbine, gearbox, and airframe are not considered.

2.1 Source Noise Description

The source noise description may, in general, come from predictions[10] or flight test data.[11, 12] In this work, recently acquired flight test data from the Airbus/Eurocopter AS350B "AStar" light utility helicopter served as the basis for the source noise description.[12] The AStar helicopter, shown in Figure 1, has a 3-blade main rotor with a blade passage frequency (BPF) of 19.5 Hz and a 2-blade tail rotor with a BPF of 104 Hz. The advancing side of the main rotor is on the port side of this vehicle. An example pressure time history from a level flyover at the Sierra Army Depot, CA test site is shown in Figure 2. Here, the vehicle was flying at an indicated airspeed of 54 m/s (105 KIAS) at an altitude of 61 m above ground level (AGL). The measurement was made using a ground plate microphone system.[12]

Figure 1 – Photograph of AStar helicopter.

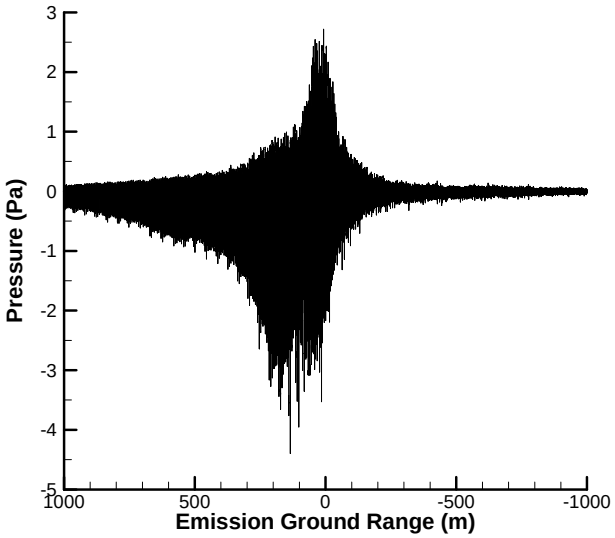

Figure 2 – Measured flyover noise at ground.

Separation of the main and tail rotor acoustic signals from the ground measurement follows the method developed by Greenwood and Schmitz.[13] Briefly, the ground microphone data and flight path data are synchronized during acquisition. This allows the ground pressure time history

to be de-Dopplerized in the time domain and corrected for spherical spreading loss, in essence creating a virtual in-flight source recording at some fixed reference distance. No attempt is made to remove the effect of atmospheric absorption since the data used in this process is acquired within a short distance (610 m) from the source, and because of the low frequency content of the source.

The resulting virtual source recording is sliced into short stationary segments, each assigned to its own emission angle. A wavelet-based method is then used to determine the main and tail rotor BPFs. With that information, each segment is sliced into a sequence of individual main rotor blade passages, block aligned, and synchronously time averaged. The resulting time-averaged main rotor signature is replicated and subtracted from the original segment. The process is then repeated at the tail rotor BPF to obtain a time-averaged tail rotor signature at its BPF. In this manner, separate main and tail rotor signatures may be obtained over a range of emission angles in both the elevation and azimuthal directions.

Shown in Figure 3 and Figure 4, for example, are the main and tail rotor signatures at the nose and 45° off the nose on the retreating side, respectively. These were obtained from data emitted at an angle 16° below the horizontal and are shown at a reference distance of 30.48 m (100 ft.). Note the relative magnitude of the main and tail rotors, and how the magnitudes vary between emission angles. For this reason, multiple angles must be considered when assessing detection range.

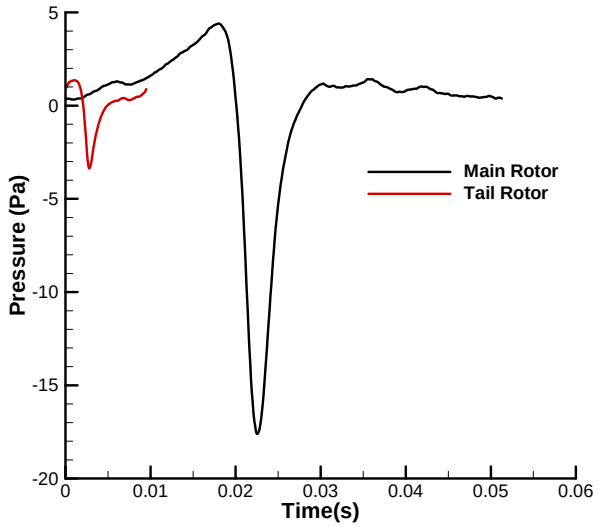

Figure 3 – Time-averaged main and tail rotor signatures at nose.

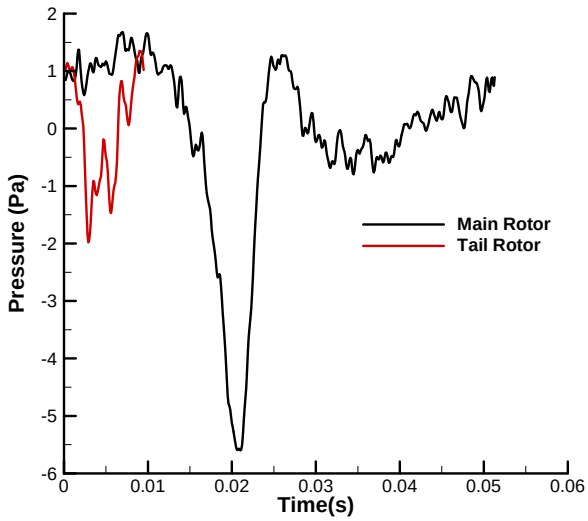

Figure 4 – Time-averaged main and tail rotor signatures on retreating side.

Finally, note that the time averaging process removes a substantial portion of the temporal variation in source noise. While lack of those variations detract from perceptual fidelity,[14] they are not desired for detection model validation studies.

2.2 Synthesis Considerations

With the source noise now characterized by separate blade passage signatures of the main and tail rotor as a function of emission angle, it is possible to synthesize long, combined pressure time histories for subsequent propagation. In the most general case of an arbitrary trajectory, the synthesis would entail morphing the signatures over time with changing emission angle. In the present case, however, the process is made simpler by the fact that the source originates at some great distance and is flying at a low altitude. For a straight-in approach, this effectively eliminates

the need to morph the signatures because the only azimuthal emission angle required is at the nose and the only (low) elevation angle required does not significantly change over the range of interest. Had the aircraft been at higher altitude with detection occurring overhead, this simplification would not be possible.

The signal generation required to determine the detection range at a particular non-zero azimuthal angle is more complicated. The brute force approach is depicted in Figure 5 in which a number of parallel sideline operations along the velocity vector $\mathbf{V}$ are simulated with decreasing normal distance to the observer. The detection range (represented by *) for the desired angle would be determined when test subjects both detected the signal and when that detection occurred at the desired angle. The approach is not desirable because it complicates the synthesis since signatures have to be morphed from one azimuthal angle to another, and because it would be inefficient for test subjects to listen to sounds at emission angles of no particular interest.

A more elegant solution is to "crab" the vehicle, i.e., fly it with its nose pointed in the direction of $\mathbf{V}$, but with its direction of travel along the desired azimuthal angle (Az) specified by the unit vector $\hat{\mathbf{r}}$, see Figure 6. This added simplification allows one to perform a detection test using a single fly-in event at the desired azimuthal angle, greatly improving the efficiency of the test and eliminating the need for morphing between different azimuthal angles.

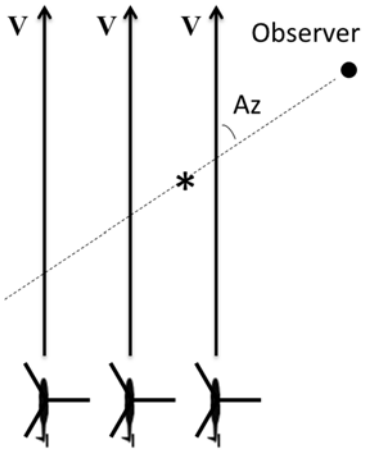

Figure 5 – Means of finding detection distance through successive parallel fly-ins.

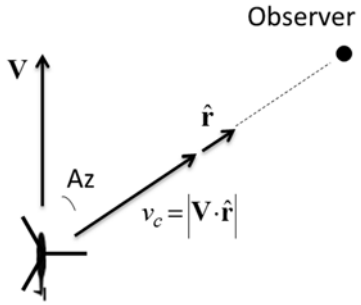

Figure 6 – Means of finding detection distance by crabbing toward observer at desired azimuthal angle.

This trick requires some consideration of the relationship between the flight speed and the Doppler shift. If the flight speed along $\hat{\mathbf{r}}$ is $v_c = |\mathbf{V} \cdot \hat{\mathbf{r}}|$, the Doppler shift factor (DSF) will be simulated during propagation processing (see Section 3) as

$$\mathrm{DSF}\big|_{\mathrm{crab}} = 1/(1 - v_c / c_0) = c_0 / (c_0 - v_c) \tag{1}$$

where c_0 is the speed of sound in air. However, taking this approach may introduce a bias during testing if there is a dependency of the detection range on the speed since v_c is different than the intended speed of $v = |\mathbf{V}|$. To mitigate this potential problem, the vehicle is flown along $\hat{\mathbf{r}}$ at the intended speed of v, and a correction is applied to the Doppler shift factor. This correction can be accomplished during synthesis by scaling the BPFs f by

$$\hat{f} = f \frac{\mathrm{DSF}\big|_{\mathrm{crab}}}{\mathrm{DSF}\big|_{\mathrm{zero\ crab}}} = f \frac{c_0 - v}{c_0 - v_c} \tag{2}$$

where $\hat{f}$ are the scaled BPFs. This has the desired effect of flying the source at speed *v*, but having the Doppler shift associated with azimuthal angle Az. In the limit, when Az = 0°, then $v_c = v$, $\hat{f} = f$, and $\mathrm{DSF} = 1/(1 - v/c_0)$. When Az = 90°, then $v_c = 0$, $\hat{f} = f(1 - v/c_0)$, and DSF = 1, i.e., no Doppler shift.

2.3 Additive Synthesis

Synthesis of combined main and tail rotor pressure time histories is performed in the time domain using an additive synthesis approach, that is,

$$p(t) = \sum_{i=1}^{m} A_i^{MR} \cos\left(2\pi \hat{f}_i^{MR} t + \varphi_i^{MR}\right) + \sum_{j=1}^{n} A_i^{TR} \cos\left(2\pi \hat{f}_i^{TR} t + \varphi_i^{TR}\right) \tag{3}$$

where *A* and φ are the amplitudes and phases of each harmonic, $\hat{f}$ are the scaled BPFs, *m* and *n* are the number of main and tail rotor harmonics, respectively, and the superscripts *MR* and *TR* denote main and tail rotor, respectively. The amplitudes and phases are obtained by performing a single FFT of the individual main and tail rotor signatures over a time window equal to their respective periods. Figure 7 shows the amplitudes of the main and tail rotor harmonics corresponding to the signatures shown in Figure 3. At this particular emission angle, the amplitudes of the tail rotor harmonics exceed the neighboring main rotor harmonics, except at the fundamental.

The pressure time histories are generated with sufficient length (typically hundreds of seconds) to allow simulated fly-ins over tens of kilometers. Note that while not exercised here, the additive synthesis method allows changes in amplitude and BPF as a function of time.[14] It also allows resampling of the waveform by specifying a sampling rate that is different from that used in the generation of the time-averaged signatures. A snippet of pressure time history corresponding to the spectra in Figure 7 is shown in Figure 8. Since the main and tail rotor BPFs are not harmonically related, their superposition gives a time-varying quality to the generated waveform that would otherwise be missing if only the main rotor was included.

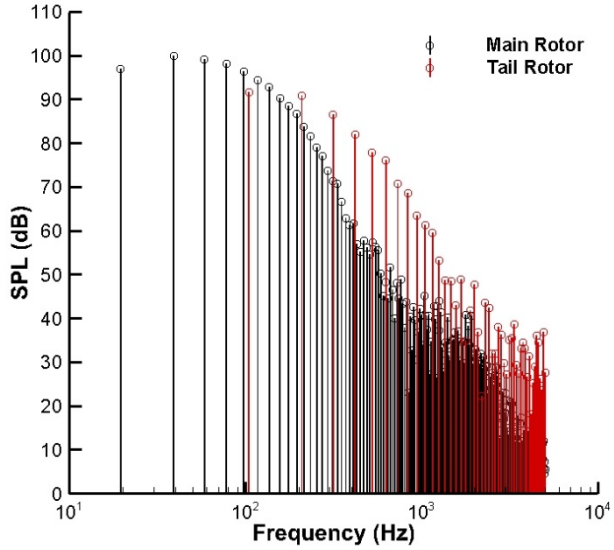

Figure 7 – Harmonics of the main and tail rotor signatures (nose).

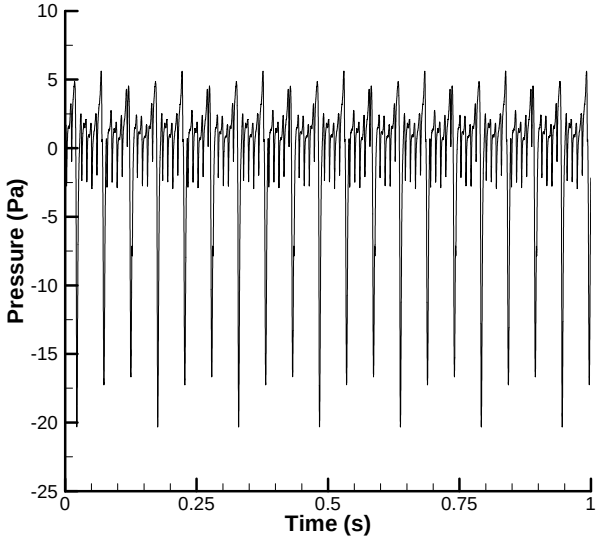

Figure 8 – Snippet of synthesized pressure time history (nose).

3 SIMULATED PROPAGATION

The process for generating a pseudo-recording at an observer near the ground entails application of a time-varying time delay, gain and filter to the synthesized source noise. Assuming a straight-line propagation path, the sound at the observer is obtained through the sum of the direct path and ground reflected path, as shown in the block diagram in Figure 9. In this work, the time dependency of each block is due to the change in the propagation path as the source moves with respect to the observer, and not due to time-varying characteristics of a fixed path, e.g., atmospheric turbulence. The digital signal processing associated with Figure 9 is performed on a dedicated audio server[15] as part of the NASA Community Noise Test Environment (CNoTE)[16] simulator application. NASA-developed model plugins were used for the atmospheric absorption and ground attenuation blocks.

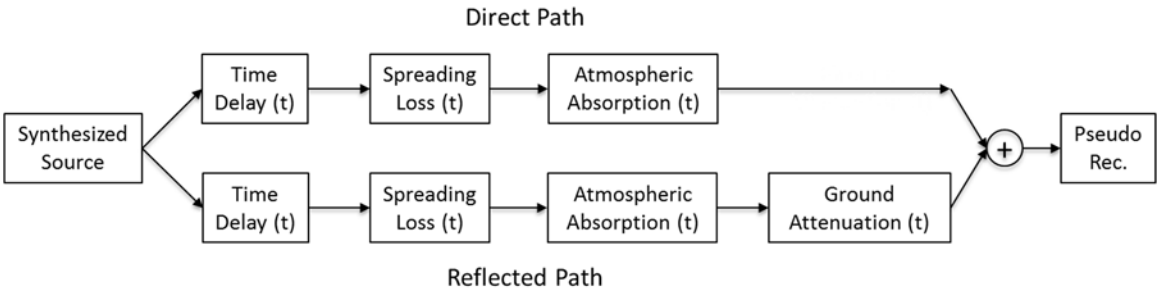

Figure 9 – Block diagram showing the signal processing steps involved in generating a pseudo-recording at the observer location from the synthesized source noise.

3.1 Time Delay, Spreading Loss and Atmospheric Absorption

Simulation of time delay, spherical spreading loss and atmospheric absorption have been discussed in other work by the authors. For brevity, they are only summarized here.

The time delay represents the absolute delay between the source emission time and receiver time. Because the time delay usually does not align with a sample, a fractional delay method must be employed.[17] The time rate of change of the delay line simulates the Doppler shift.[18] The aforementioned Doppler correction therefore needs to be applied during synthesis in order to simulate the Doppler shift corresponding to the desired crab angle. The interference caused by the addition of the propagated direct and reflected rays produces a comb-filter effect,[19] which alters the spectral content in a time-varying manner as the aircraft moves along its trajectory.

The spherical spreading loss specifies a time-varying gain and is computed as the ratio of the reference distance by the instantaneous slant range, i.e., the straight-line distance between the emission position and the observer.

Atmospheric absorption is accumulated at each 1⁄3-octave band center frequency along the straight-line path through the specified atmosphere. The absorption curve is fit with a 2^n-point spline and converted to a minimum-phase finite impulse response (FIR) filter via a real cepstrum, as described by Rizzi et al.[18] For a uniform atmosphere, the filter is slant-range-dependent and therefore varies in time with the moving source.

3.2 Ground Attenuation

Incorporation of an appropriate ground plane attenuation model for the reflected path is critical for this application as it has a significant effect on the sound received by the observer. The

reflected path is handled using a virtual image source specified at a height H_{src} below the ground plane, as depicted in Figure 10. For a plane wave incident at angle ϕ on a locally reacting ground plane, the complex reflection coefficient R_p is given as[20]

$$R_p = \frac{\sin\phi - Z_1/Z_2}{\sin\phi + Z_1/Z_2} \tag{4}$$

where $Z_1 = \rho_0 c_0$ is the characteristic impedance of air, and Z_2 is the acoustic impedance of the ground. In this work, the Attenborough four-parameter model is used to specify the ground impedance, however other models are available.[21] In the Attenborough model, the ground impedance is given as

$$Z_2 = \frac{\omega \rho_b(\omega)}{k_b} \tag{5}$$

where $\omega = 2\pi f$, f is the frequency in Hz, and

$$\rho_b(\omega) = \rho_0 \frac{q^2}{\Omega}\left[1 - 2\frac{T(\lambda\sqrt{i})}{\lambda\sqrt{i}}\right]^{-1}, \qquad k_b^2 = k^2 q^2 \left[1 - 2\frac{T(\lambda\sqrt{i})}{\lambda\sqrt{i}}\right]^{-1}\left[1 + 2(\gamma - 1)\frac{T(\sqrt{N_{pr}}\lambda\sqrt{i})}{\sqrt{N_{pr}}\lambda\sqrt{i}}\right]$$

$$\lambda = \frac{1}{s_f}\sqrt{\frac{8\rho_0 q^2 \omega}{\Omega\sigma}}, \qquad q^2 = \Omega^{-g}, \qquad T(x) = \frac{J_1(x)}{J_0(x)}. \tag{6}$$

As presented, the wavenumber k_b is not normalized by the wavenumber in air $k = \omega / c_0$, and this form differs from Eqn. (8) in Attenborough.[21] In the above, $J_0(x)$ and $J_1(x)$ are the 0th and 1st order cylindrical Bessel functions, N_{pr} is the dimensionless Prandtl number, and the four parameters are the dimensionless grain shape factor g, the dimensionless pore shape factor ratio s_f, the dimensionless volume porosity Ω and the flow resistivity σ.

Under the plane wave assumption, the pressure at the observer is given by[20]

$$\frac{p}{p_0} = \frac{1}{r_1}e^{-ikr_1} + \frac{R_p}{r_2}e^{-ikr_2} \tag{7}$$

where the denominator of the first and second terms on the right hand side are the aforementioned spherical spreading loss for the direct and ground reflected waves, respectively. It is noted that for small ϕ, $\sin\phi \ll Z_1/Z_2$, and R_p approaches -1. This results in a non-physical cancellation of the direct and ground reflected waves for any finite ground impedance. In this case, the plane wave assumption is invalid and a spherical wave correction must be applied to Eqn. (7), giving[20]

$$\frac{p}{p_0} = \frac{1}{r_1}e^{-ikr_1} + \frac{R_p}{r_2}e^{-ikr_2} + (1 - R_p)\frac{F}{r_2}e^{-ikr_2} \tag{8}$$

where the boundary loss factor F and the numerical distance w are given by[22, 23]

$$F = 1 + i\sqrt{\pi} w e^{-w^2}\operatorname{erfc}(-iw), \qquad w = \sqrt{\frac{1}{2}ikr_2}\left(\sin\phi + \frac{Z_1}{Z_2}\right) \tag{9}$$

and erfc() is the complementary error function. The solution to the expression for the boundary loss factor is facilitated by recognizing the term $e^{-w^2}\text{erfc}(-iw)$ as the Faddeeva function, for which numerous tabular and software solutions are available.[24]

Figure 11 shows the sound pressure level (SPL) computed with the plane wave assumption, Eqn. (7), subtracted from the SPL computed with the spherical correction, Eqn. (8), at several lateral distances of the source. The source height is fixed at 30.48 m and the observer height is 0 m. The ground surface had an acoustic impedance similar to compressed dirt, referred to as "old dirt road",[25] with the four parameters of the Attenborough model given by σ = 3 MPa-s/m^2, g = 0.75, s_f = 0.875, and Ω = 0.715. A uniform atmosphere at a temperature of 15 °C was used giving c_0 = 340.27 m/s, with ρ_0 = 1.225 kg/m^3 and N_{pr} = 0.724. It is clear from Figure 11 that at high elevation angles corresponding to distances of 30.48 – 304.8 m, the difference in ground attenuation is negligible. However, at lower angles, corresponding to greater distances, the differences are greater. In particular, the plane wave assumption substantially overestimates the attenuation, and it does so in a frequency range that is significant for the source under consideration. Consequently, simulations based on the plane wave assumption will generally indicate significantly smaller detection ranges than those using the spherical correction.

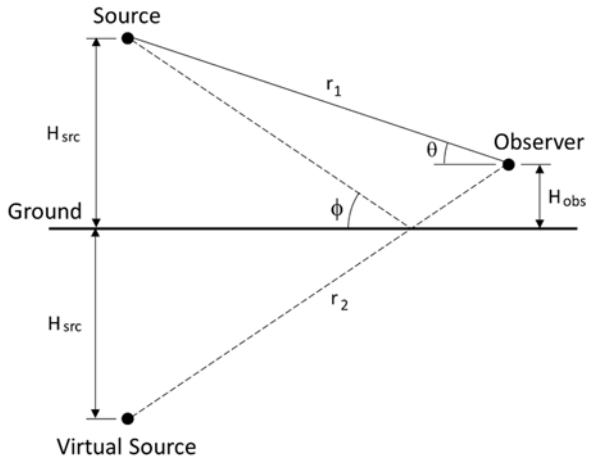

Figure 10 – Image source model used for handling ground plane reflection.

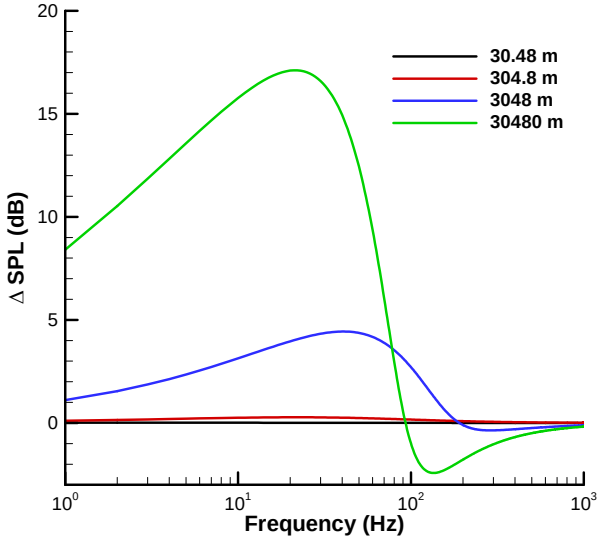

Figure 11 – Difference between SPL computed using plane and spherical wave.

With respect to the simulation itself, the image source is filtered in the time domain by a FIR filter obtained via an inverse FFT of the function $R_p + (1 - R_p)F$. The impulse response so obtained is circularly shifted in the time domain prior to the filtering operation. This produces a linear phase filter with its peak at the middle tap. A time delay t_d of

$$t_d = \frac{F_{len}}{2F_s}\text{DSF} \tag{10}$$

is subtracted from the time delay of the reflected path to compensate for the extra delay associated with the linear phase filter. The Doppler shift factor DSF is as specified in Eqn. (1). This added operation synchronizes the reflected path with the direct path. For an audio sampling rate F_s of 44100 samples/s, a minimum filter length F_{len} of 4096 is needed to define the frequency response such that there is at least one non-zero frequency bin below the BPF. As indicated in Figure 9, the filter is path dependent and therefore varies in time for a moving source.

4 RESULTS

Fly-ins were simulated for a number of ground surfaces to demonstrate the dramatic effect the ground impedance has on the sound at the receiver location. In each case, a uniform atmosphere at a temperature of 15 °C, pressure of 1 atmosphere, 50% relative humidity, density of 1.225 kg/m^3 and Prandtl number of 0.724 was specified. The AStar vehicle was "flown" at an altitude of 30.48 m AGL and indicated airspeed of 54 m/s (105 KIAS) in the direction of the observer. The altitude difference between the simulation and the baseline recording was small, so no changes were made to the source noise characteristics. The observer is at height of 1.2 m.

For each case, three of the four ground impedance parameters were fixed at g = 0.75, s_f = 0.875, Ω = 0.715. Only the flow resistivity σ was changed between surfaces, and these were set to 10 MPa-s/m^2 for "new asphalt," 3 MPa-s/m^2 for "old dirt road," 550 kPa-s/m^2 for "roadside dirt" and 200 kPa-s/m^2 for grass.[25] In addition, the limiting case of an infinitely rigid ground was simulated by eliminating the ground attenuation filter entirely, but retaining the remaining signal processing blocks associated with the reflected path.

Plotted in Figure 12 is the pseudo-recording of a fly-in with an "old dirt road" ground impedance. As is the case with other ground surfaces, a monotonic increase in level with decreasing emission distance is indicated. This well-behaved character is in contrast to the level fluctuations observed in measured long-range flight test data, making the simulated recording ideal for use in human detection studies. Figure 13 shows the un-weighted overall SPL as a function of distance for the five ground surfaces. In a typical range of interest, the difference in SPL between surfaces is as much as 17 dB (between rigid and grass). Because of low atmospheric absorption in this frequency range, that would imply almost three range doublings would be needed for spherical spreading to make up for the difference. These level differences decrease with decreasing emission distance. Supplemental audio clips of the fly-in noise corresponding to Figure 13 at two emission distances are available for download via the Internet.[26]

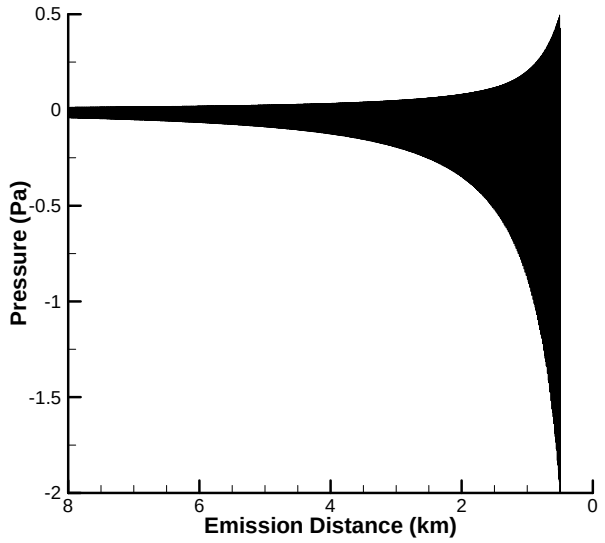

Figure 12 – Pseudo-recording of fly-in with an "old dirt road" impedance (nose).

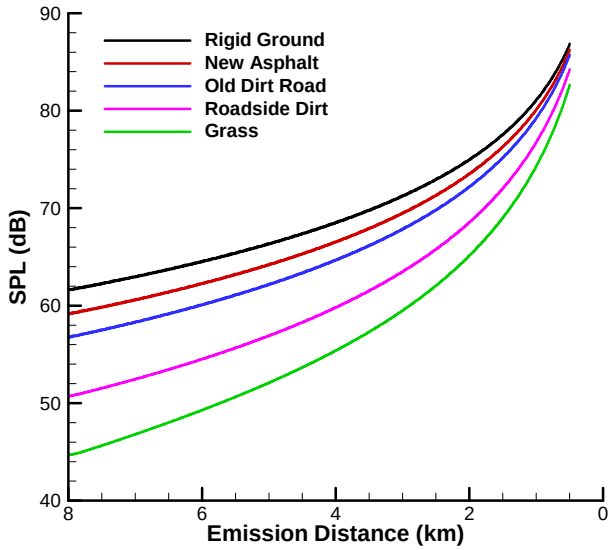

Figure 13 – Comparison of overall SPL for five ground impedances.

It is worthwhile to note that different ground impedances affect not only the overall level, but also the spectral content. Shown in Figure 14 and Figure 15 are the observed spectra for rigid and grass ground surfaces at 8 km and 2 km distances, respectively. Here it is seen that differences

between the spectra are both a function of frequency and emission distance. Hence, there are no shortcuts, e.g., gain as a function of distance, that can be applied to a pseudo-recording obtained using a simple rigid ground model to represent another ground impedance. The importance of that cannot be overlooked because spectral levels (along with other factors including the minimal audible field and background noise) have a strong influence on human detection.[7-9]

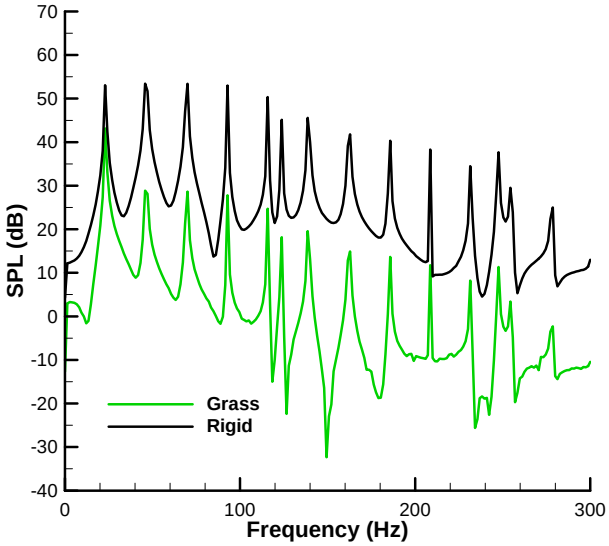

Figure 14 – Observed spectra at 8 km over grass and rigid ground surfaces.

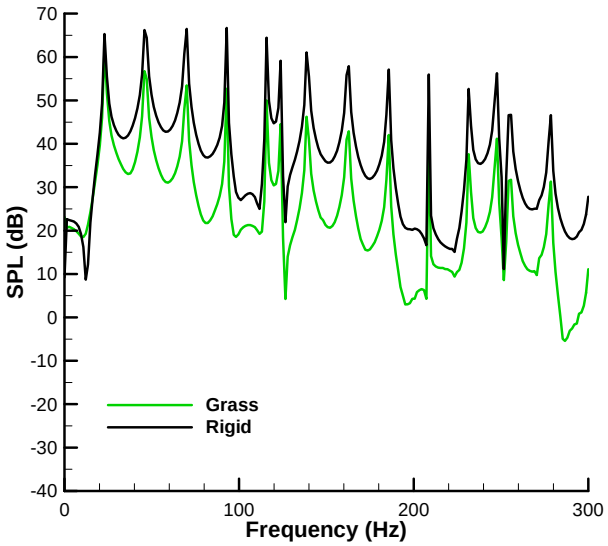

Figure 15 – Observed spectra at 2 km over grass and rigid ground surfaces.

5 DISCUSSION

A method has been developed to simulate rotorcraft fly-in noise using single blade passage signatures of the main and tail rotors. These may be obtained from flight test data (as demonstrated) or predictions. The simulation requires synthesis of long duration source noise pressure time histories, and the propagation of that noise to an observer uses physical models of the time delay, spherical spreading, atmospheric absorption, and ground plane attenuation. The latter was shown to be particularly important for this application as large differences in both level and spectral content were noted between plane and spherical wave assumptions, and between ground plane model parameters used. Further, such differences are known to influence human aural detection.

The pseudo-recordings generated by this approach are well suited for human subject testing. The low frequency reproduction capabilities of the NASA Langley Research Center Exterior Effects Room[27] allow simultaneous presentation of the approaching rotorcraft sound with a synthesized or recorded ambient. This makes it possible to understand the effect of design or operational changes on audibility in a well-controlled laboratory test environment.

6 ACKNOWLEDGEMENTS

This research was supported by the National Aeronautics and Space Administration, Aeronautics Research Mission Directorate, Advanced Air Vehicles Program, Revolutionary Vertical Lift Technology Project. The authors would like to acknowledge Brian Tuttle, Analytical Mechanics Associates Inc., Hampton, Virginia, for his significant contributions to the development of the ground attenuation plugin.

7 REFERENCES

1. "Special flight rules area in the vicinity of Grand Canyon National Park: Actions to substantially restore natural quiet," National Park Service, US Department of the Interior, Draft Environmental Impact Statement DES 10-60, (2011).

2. "Report on the Los Angeles Helicopter Noise Initiative," Federal Aviation Administration (2013).

3. "The New York North Shore Helicopter Route," Federal Aviation Administration, Department of Transportation, 14 CFR Part 93, Docket No. FAA-2010-0302, (2010).

4. Arnold W. Mueller, Charles D. Smith, Kevin P. Shepherd, and Brenda M. Sullivan, "A new version of the helicopter aural detection program, ICHIN," NASA TM-87745, (1986).

5. Kenneth J. Plotkin, "The role of aircraft noise simulation models," *InterNoise 2001*, The Hague, The Netherlands, (2001).

6. Eric R. Boeker, Eric Dinges, Bill He, Gregg Fleming, Christopher J. Roof, Paul J. Gerbi, Amanda S. Rapoza, and Justin Hemann, "Integrated Noise Model (INM) Version 7.0 Technical Manual," FAA AEE-08-01, (2008).

7. L. Hartman and H. Sternfeld, "An experiment in aural detection of helicopters," US Army Air Mobility R&D Laboratory, Ft. Eustis, VA, USAAMRDL Technical Report 13.50 under Contract DAAJ02-71-C-0065, AD917355, (1973).

8. Louis A. Abramanson, "Correlation of actual and analytical helicopter aural detection criteria, Volume 1," US Army Air Mobility R&D Laboratory, Ft. Eustis, VA, USAAMRDL-TR-74-102A, (1975).

9. D.M. Green and J.A. Swets, *Signal Detection Theory and Psychophysics*. New York, John Wiley and Sons, Inc., (1966).

10. Kenneth S. Brentner and Feridoun Farassat, "Modeling aerodynamically generated sound of helicopter rotors," *Progress in Aerospace Sciences*, **39**, 83-120, (2003).

11. Michael E. Watts, David A. Conner, and Charles D. Smith, "Joint Eglin Acoustic Week III Data Report," NASA TM–2010-216206, (2010).

12. James H. Stephenson and Eric Greenwood, "Effects of vehicle weight and true versus indicated airspeed on BVI noise during steady descending flight," *AHS 71st Annual Forum*, Virginia Beach, VA, (2015).

13. Eric Greenwood and Fredric H. Schmitz, "Separation of main and tail rotor noise from ground-based acoustic measurements," *AIAA Journal of Aircraft*, **51**(2), 464-472, (2014).

14. Jonathan R. Hardwick, Andrew Christian, and Stephen A. Rizzi, "Evaluation of the perceptual fidelity of a novel rotorcraft noise synthesis technique," *Journal of the Acoustical Society of America*, **136**(4), 2287, (2014).

15. "GoldServe, AuSIM3D Gold Series Audio Localizing Server System, User's Guide and Reference, Rev. 1d," AuSIM Inc., Mountain View, CA, October (2001).

16. Stephen A. Rizzi, Brenda M. Sullivan, and Aric R. Aumann, "Recent developments in aircraft flyover noise simulation at NASA Langley Research Center," *NATO Research and Technology Agency AVT-158 "Environmental Noise Issues Associated with Gas Turbine Powered Military Vehicles" Specialists' Meeting*, NATO RTA Applied Vehicle Technology Panel, Paper 17, Montreal, Canada, (2008).

17. T. I. Laakso, V. Välimäki, M. Karjalainen, and U.K. Laine, "Splitting the Unit Delay -Tools for Fractional Delay Filter Design," *IEEE Signal Processing Magazine*, **13**, 30-60, (1996).

18. Stephen A. Rizzi and Brenda M. Sullivan, "Synthesis of virtual environments for aircraft community noise impact studies," *11th AIAA/CEAS Aeroacoustics Conference*, AIAA-2005-2983, Monterey, CA, May, (2005).

19. Pierre Dutilleaux and Udo Zölzer, "Delays", Chap. 3 in *DAFX - Digital audio effects*, edited by Udo Zölzer, John Wiley & Sons, Ltd., West Sussex, England, (2002).

20. Joseph E. Piercy, Tony F.W. Embleton, and Louis C. Sutherland, "Review of noise propagation in the atmosphere," *Journal of the Acoustical Society of America*, **61**(6), 1403-1418, (1977).

21. Keith Attenborough, "Acoustic impedance models for outdoor ground surfaces," *Journal of Sound and Vibration*, **99**(4), 521-544, (1985).

22. Keith Attenborough, Sabih I. Hayek, and James M. Lawther, "Propagation of sound above a porout half-space," *Journal of the Acoustical Society of America*, **68**(5), 1493-1501, (1980).

23. K.B. Rasmussen, "Sound propagation over grass covered ground," *Journal of Sound and Vibration*, **78**(2), 247-255, (1981).

24. "Faddeeva function," http://en.wikipedia.org/wiki/Faddeeva_function, Wikipedia, Date Accessed April 26, (2015).

25. Tony F.W. Embleton and Gilles A. Daigle, "Atmospheric Propagation", Chap. 12 in *Aeroacoustics of Flight Vehicles: Theory and Practice. Volume 2: Noise Control*, edited by Harvey H. Hubbard, NASA RP 1258, Hampton, VA, (1991).

26. "Aircraft flyover simulation," http://stabserv.larc.nasa.gov/flyover/, NASA, (2015).

27. Kenneth J. Faller II, Stephen A. Rizzi, and Aric R. Aumann, "Acoustic performance of a real-time three-dimensional sound-reproduction system," NASA TM-2013-218004, June (2013).